(Received 23 November 2024, Accepted 1 January 2025, Scheduled 17 January 2025)

Compact 3D Printed Double-Ridged Conical Horn Antenna for Breast Tumour Detections Utilizing Microwave Imaging over Ultra-Wideband Regime

Athul O. Asok and Sukomal Dey*

Department of Electrical Engineering, Indian Institute of Technology Palakkad, Kerala-678623, India

ABSTRACT: This paper presents a new 3D-printed, compact Double-Ridged Conical Horn (DRCH) antenna designed for Ultra-Wideband (UWB) Microwave Imaging (MI). The performance of the proposed antenna is analyzed using an electromagnetic (EM) solver, which demonstrates favorable return loss, gain, and radiation characteristics, indicating its structural and performance robustness. To validate the final design, a prototype is fabricated and tested experimentally. The proposed model features reduced dimensions compared to traditional and commercially available Dual Ridge Horn (DRH) antennas, while still maintaining a broad operational bandwidth ($|S_{11}| > -10$ over the 0.69 GHz–12 GHz range). Within the variety of potential applications, this frequency band is particularly suitable for biomedical devices, particularly in MI, where compact size is crucial for seamless integration into these systems. Additionally, a safety evaluation of the designed antenna has shown that its Specific Absorption Rate (SAR) is well below regulatory limits, ensuring that it can be safely operated near human users.

1. INTRODUCTION

Breast cancer is recognized as a significant cause of mortality among women worldwide, with the highest incidence rates [1]. Early detection is crucial in reducing its mortality rates. Current strategies emphasize extensive screening campaigns targeting women to detect the disease in its initial stages, when conventional treatments like chemotherapy and radiotherapy are highly effective. X-ray mammography is a widely used screening technique due to its sensitivity, despite its considerable false positive rate. However, mammography's drawbacks include its comparative invasiveness, requiring substantial breast compression for adequate image quality and the use of ionizing radiation [2].

Microwave Imaging (MI) has emerged as a viable and innovative technique, offering a safe alternative to traditional methods by utilizing low-power and non-ionizing radiation [3–7]. Unlike mammography, MI is noninvasive, eliminating the need for painful breast compression, making it a patient-friendly and cost-efficient option for breast cancer detection [8–10]. These benefits make MI a potential diagnostic solution for integration into hospitals.

MI can be performed either using a broadband signal or a single-frequency excitation pulse [7]. Ultra-Wideband (UWB) MI has a long history as a reliable method for detecting inhomogeneities in biological tissues. This technique involves illuminating the target area with brief, low-power microwave pulses from a specially designed transmitting antenna or array of antennas. The scattered signals are then captured by the receiving elements and processed to generate spatial maps that reveal the target's size and location, making it highly effective for identifying cancerous nodules [11–16].

Designing MI systems involves selecting the appropriate antenna type. Various antenna designs have been proposed, including dipole and monopole antennas, Vivaldi antennas, horn antennas, and bow-tie configurations [17–19]. Additionally, metasurfaces have been widely employed to enhance antenna performance for biomedical applications [20–24]. The choice of antenna type depends on the specific requirements of the experimental setup, with a wide frequency band and directional radiation being necessary for high-resolution imaging and mitigation of environmental effects [25]. These requirements translate into the need for effective impedance matching, low signal distortion, and a stable radiation pattern and gain across frequencies.

However, achieving a wide operating bandwidth, unidirectional radiation and compact size in an antenna for MI remains a significant challenge. The limited space available in MI applications, such as breast cancer detection, necessitates minimizing the antenna size. This manuscript focuses on designing and implementing a compact transmitting antenna for integration into an MI system for breast cancer detection.

Dual-Ridged Conical Horn (DRCH) antennas are well suited for the use in UWB MI due to their broad bandwidth and appropriate radiation patterns. However, commercially available Double-Ridged Horn (DRH) antennas [26, 27] are typically too large for seamless integration into a standard MI system. Therefore, a novel 3D-printed DRCH is proposed that achieves wide bandwidth and directional radiation patterns suitable for MI. A prototype was fabricated to validate the theory and simula-

* Corresponding author: Sukomal Dey (sukomal28@gmail.com).

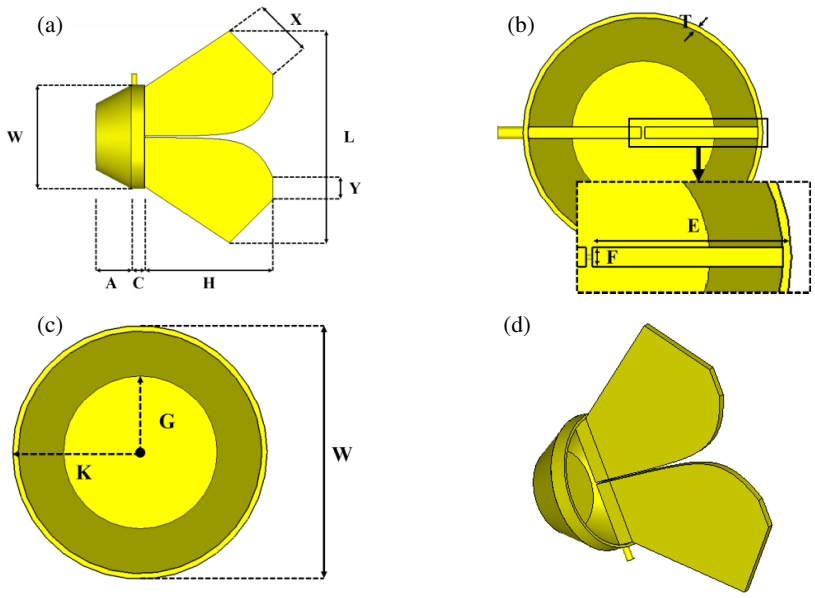

FIGURE 1. The different cross sections of the developed DRCH antenna. (a) Top view of the antenna, (b) cavity section with the feed, (c) frustum shaped cavity and (d) perspective view of the device.

tions, demonstrating the feasibility of the proposed 3D-printed DRCH antenna. The fabricated device was then utilized to image cancerous cells embedded in a laboratory-developed heterogeneous breast phantom, demonstrating the utility of the DRCH for imaging.

The manuscript is structured as follows. Section 2 covers the general theoretical aspects and provides an in-depth analysis of the design, simulation, and experimental work involving the proposed antenna. In Section 3, the development of the breast phantom in the simulator is presented, along with various performance analyses, including Specific Absorption Rate (SAR), E-field plots, H-field plots, power flow density, and Near-Field Directivity (NFD). Section 4 focuses on the breast phantom fabrication and its imaging. The paper concludes with a summary in Section 5.

The novelties of this research are as follows:

1. To the best of the authors' knowledge, the developed 3D-printed DRCH antenna is lightweight, low-cost, and operates from 0.69 GHz to 12 GHz, with a peak gain of 14 dBi at 12 GHz.
2. Comprehensive analyses, including SAR, E-field distribution, H-field distribution, power flow density, and NFD, have been conducted in the proposed work.
3. A heterogeneous breast phantom with two tumors has been developed to evaluate the imaging capability of the antenna using the fundamental Delay and Sum (DAS) algorithm with monostatic and bistatic approaches.
4. The developed 3D-printed DRCH antenna has been compared with a range of antennas reported in the literature to evaluate its performance, characteristics, and suitability for breast tumor detection.

2. THEORETICAL ASPECTS AND ANTENNA DESIGN

The proposed antenna design is based on the conventional structure of a traditional DRCH, as depicted in Fig. 1 [28]. Given the focus on MI for breast cancer detection, it is important to note that the UWB frequency is particularly useful. This frequency range balances achieving sufficient penetration depth within breast tissues and providing the necessary spatial resolution. The literature indicates that MI for breast cancer can achieve a resolution limit of $\lambda/4$ [29]. Therefore, all design decisions are aimed at meeting these key requirements.

Figure 1(a) shows the top view of the developed antenna. A notable modification introduced in this study, compared to [28], is the removal of the conical flares in the E- and H-planes. This design choice results in a lower operational frequency for the antenna. This aspect is particularly significant, as achieving a lower operational frequency while maintaining compact dimensions is inherently challenging. As the antenna dimensions approach the wavelength, radiating efficiency tends to decrease.

The ridge profile is another critical factor that significantly influences antenna performance. In the initial phase of the simulation, an exponential taper profile was used, which facilitated excellent impedance matching between the waveguide section and free space. From this exponential profile, the corners of the flares were trimmed as depicted in Fig. 1(a) to further improve the lower cutoff frequency of the developed DRCH. The linear segment in the ridges, when being superimposed on the exponential section, results in a significant improvement in impedance matching at lower frequencies. As also evident from Fig. 1(a), the linear segment of the ridge profile starts at the position of the feed line and extends towards the end of the cylindrical section, covering a length of C mm, whereas the exponential segment begins at the end of the cylindrical section and extends to the end, covering a total length of H mm.

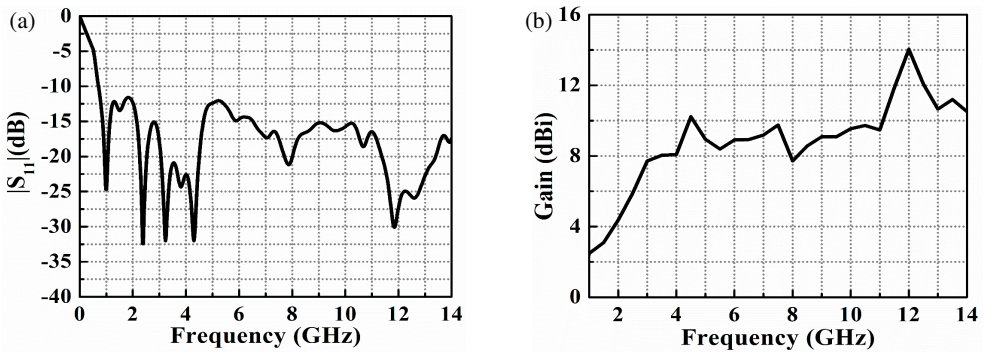

FIGURE 2. The simulated (a) return loss plot and (b) gain plot.

Figure 1(b) illustrates the back cavity section with the attached feed. In this setup, a standard 50 Ω coaxial cable connects the Vector Network Analyzer (VNA) to the antenna. The inner conductor is connected to the bottom ridge via a hole in the top ridge as depicted in the figure [30, 31]. This design approach offers several advantages: it ensures mechanical robustness of the electrical contact, facilitates easier impedance matching, and effectively suppresses higher-order modes.

The conical back cavity of the DRCH is depicted in Fig. 1(c). The cavity section is shaped like a frustum of a cone with a thickness of T mm. The height of the frustum is A mm, with the smaller radius G mm and larger radius K mm. The dimensions of the cavity have been carefully adjusted to achieve optimal performance. The complete antenna design and analysis were conducted using the electromagnetic solver CST Microwave Studio 2018. The antenna has been thoroughly optimized to achieve the desired bandwidth and ensure appropriate radiation characteristics for MI. The final dimensions of the designed antenna are provided in Table 1 for reference.

TABLE 1. The optimized dimensions of the DRCH antenna.

Parameter	Dimension (mm)	Parameter	Dimension (mm)
L	193.8	G	30.5
W	95	K	47.5
H	122.3	X	56.4
C	12	Y	19.5
A	32	O	100
T	2	P	12
E	46.8	U	55
F	4.5	V	193.8

2.1. Frequency Domain Analysis

The return loss plot on the designed antenna has been observed from the simulator. It has been found that the proposed antenna operates from 0.69 GHz to 12 GHz, depicted clearly in Fig. 2(a). The gain performance of the antenna has been observed and depicted in Fig. 2(b). It can be observed from the figure that the proposed antenna achieves a peak gain around 14 dBi at 12 GHz.

Once the antenna design was completed, the proposed design was fabricated using 3D printing technology. The 3D printing approach was chosen for its excellent balance of cost, machinability, and lightweight properties, which are crucial for effective use in an MI system. The complete antenna was printed in three stages. The first stage included the cylindrical section with the feed section and ridges. The second stage involved the back cavity section. These two stages were separately printed using ABS plastic material. Additionally, the dielectric cylinder between the inner conductor and ground was printed as the final stage.

After the printing stage, the first two sections were coated with adhesive copper tape to make the surface conductive. Extra care was taken to ensure that the surface was as smooth as possible. The two sections, after copper coating, were merged to form the final antenna structure. The dielectric cylindrical rod was inserted inside the port section before placing the inner conductor. A female SMA connector was attached to the port section to facilitate connection with the coaxial cable for testing. Fig. 3(a) depicts the first 3D-printed stage. The 3D-printed cylindrical cavity is shown in Fig. 3(b), and the 3D-printed cylindrical dielectric is shown in Fig. 3(c). The final fabricated antenna is depicted in Fig. 4, where Fig. 4(a) shows the front view; Fig. 4(b) shows the side view; and Fig. 4(c) provides the perspective view of the developed antenna. The complete measurement setup is shown in Fig. 5(a), and the antenna mounting station is separately depicted in Fig. 5(b) for clarity. The fabricated antenna was weighed, as shown in Fig. 5(c), and it was observed that the antenna weighs 134.75 g.

The simulated and measured return losses of the proposed antenna were plotted and depicted in Fig. 6(a), while the simulated and measured gains were plotted and depicted in Fig. 6(b). The simulated and measured radiation patterns of the proposed antenna were observed in the E- and H-planes at various frequencies to understand the antenna's radiation properties. The E-plane radiation pattern was observed at (a) 3 GHz, (b) 5 GHz, (c) 7 GHz, and (d) 8 GHz, as depicted in Fig. 7. The H-plane radiation pattern was observed at the same frequencies and is depicted in Fig. 8.

From the figures, it can be observed that the antenna produces a directional radiation pattern, which is crucial for biomedical imaging applications. Overall, there is a good

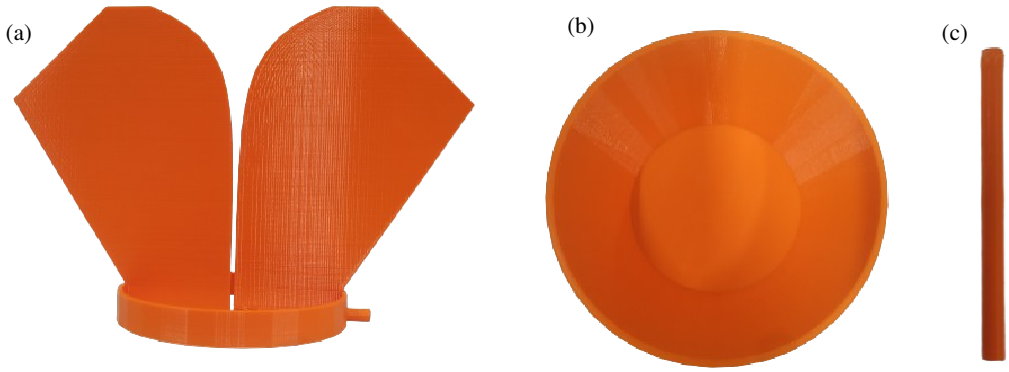

FIGURE 3. The fabricated 3D printed DRCH antenna parts. (a) The ridges along with the feed section, (b) conical back cavity and (c) cylindrical rod.

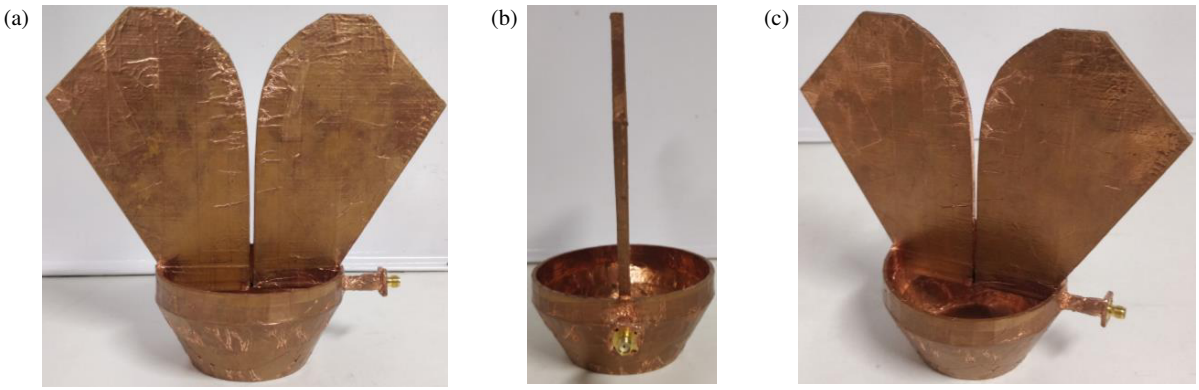

FIGURE 4. The fabricated 3D printed DRCH antenna. (a) Front view, (b) side view and (c) perspective view.

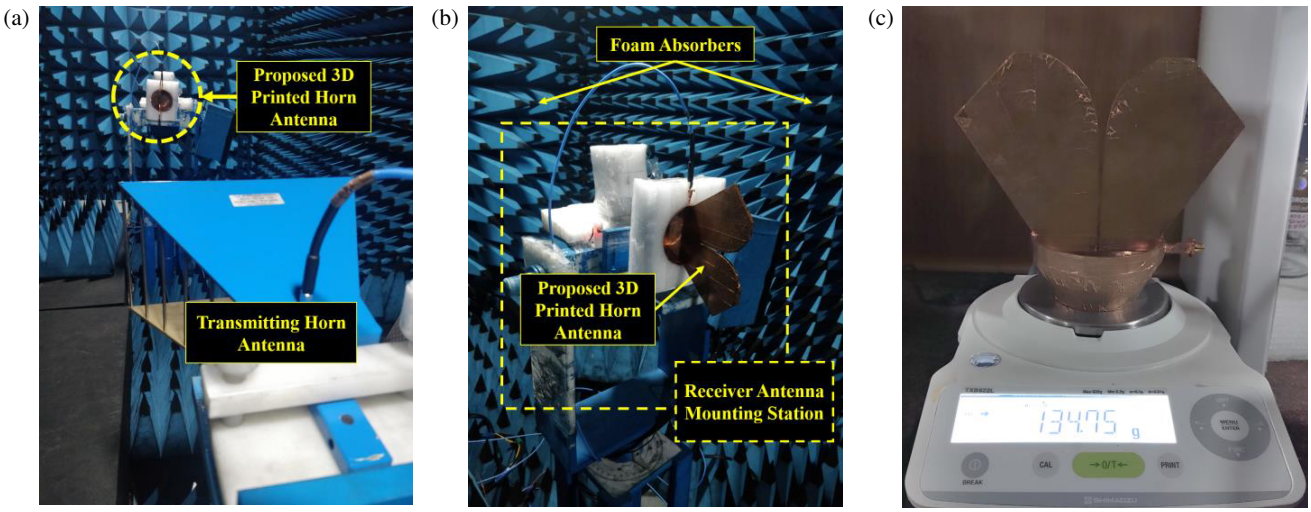

FIGURE 5. The measurement setup in this work. (a) Total setup, (b) antenna mounting station and (c) antenna weight testing unit.

correlation between the simulated and measured readings. The slight mismatches between the simulated and measured readings are attributed to minor errors in the attachment of the female SMA connector to the antenna, the surface roughness of the antenna, slight misalignments during mounting in the anechoic chamber, and the use of a PLA-based dielectric cylinder instead of Teflon.

2.2. Time Domain Analysis

To determine the appropriateness of the 3D-printed DRCH antenna for MI, a detailed investigation of its time-domain characteristics is required. This study takes into account a variety of parameters, including the transmitted-received signal, fidelity factor, and group delay. Two configurations were evaluated to determine the antenna's signal shaping capabilities and poten-

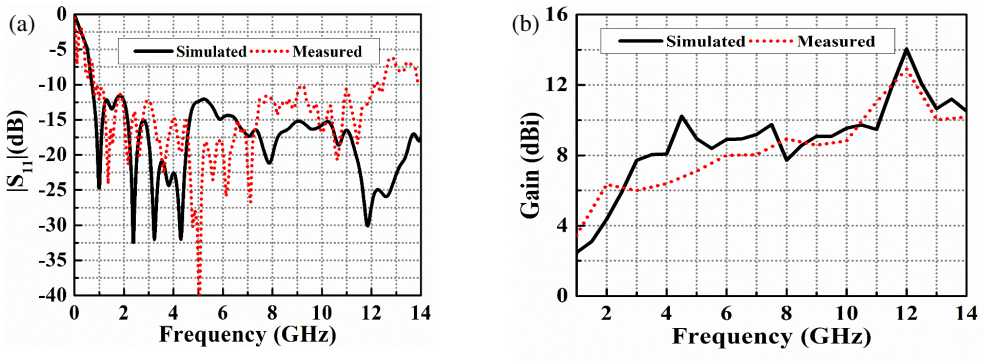

FIGURE 6. The comparison of the simulated antenna response with measured readings. (a) Return loss plot and (b) gain plot.

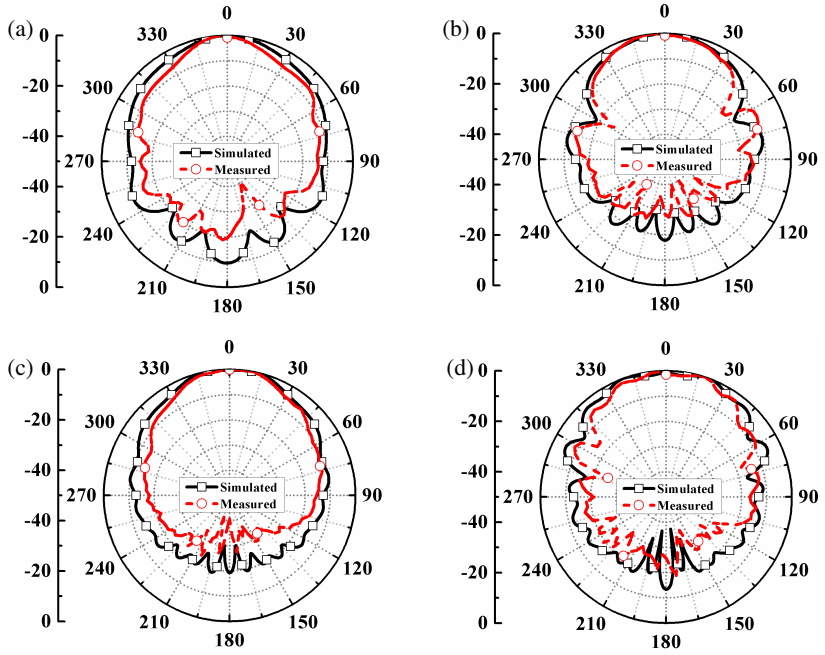

FIGURE 7. The simulated and measured E-plane radiation patterns of the proposed antenna at (a) 3 GHz, (b) 5 GHz, (c) 7 GHz, and (d) 8 GHz.

tial signal distortion: Front-To-Front (FTF) and Side-By-Side (SBS), with a 200 mm gap between the transmitter and receiver antennas. Fig. 9(a) depicts the FTF arrangement, whereas Fig. 9(b) shows the SBS configuration. Fig. 10(a) shows the normalized magnitude as a function of time for the FTF arrangement, whereas Fig. 10(b) does the same for the SBS layout. In the FTF position, the received signal closely resembles the generated signal, indicating strong directed radiation. This suggests that the FTF configuration is more effective and is recommended for breast imaging applications compared to the SBS configuration.

The cross-correlation between the transmitted and received signals is calculated using Equation (1) known as Fidelity Factor (FF) [32]. This factor measures the similarity and accuracy between the transmitted and received signals.

$$FF = \max_{\tau} \left| \frac{\int_{-\infty}^{+\infty} S(t)\, r(t-\tau) dt}{\int_{-\infty}^{+\infty} S(t)^2 . \int_{-\infty}^{+\infty} r(t)^2 dt} \right| \quad (1)$$

where $s(t)$ and $r(t)$ represent transmitted and received signals, respectively, and τ denotes the Group Delay (GD). The FF values for each antenna arrangement are as follows: 85% for the FTF layout and 37% for the SBS configuration. The high FF value in the FTF configuration implies that the transmitted signal is less distorted.

GD is a crucial aspect in evaluating the time-domain performance of the antenna since it quantifies the phase distortion of the signal. The GD is the negative rate of change of the phase of the transfer function, denoted as $\phi(\omega)$, with respect to frequency [32]. It represents the duration needed for a signal to travel through the antenna. The calculation of the GD can be determined by utilising Equation (2) in the following manner:

$$\tau(\omega) = -\frac{\mathrm{d}\varphi(\omega)}{\mathrm{d}\omega} = -\frac{\mathrm{d}\varphi(\omega)}{2\pi \mathrm{df}} \quad (2)$$

Fig. 11 depicts the simulated GD in this work using two distinct setups (FTF and SBS). The GD variations for the FTF design are within an acceptable range of up to 2.4 ns; however, the SBS configuration exhibits noticeable distortion. The FTF design is the recommended configuration for MI, considering both FF and GD.

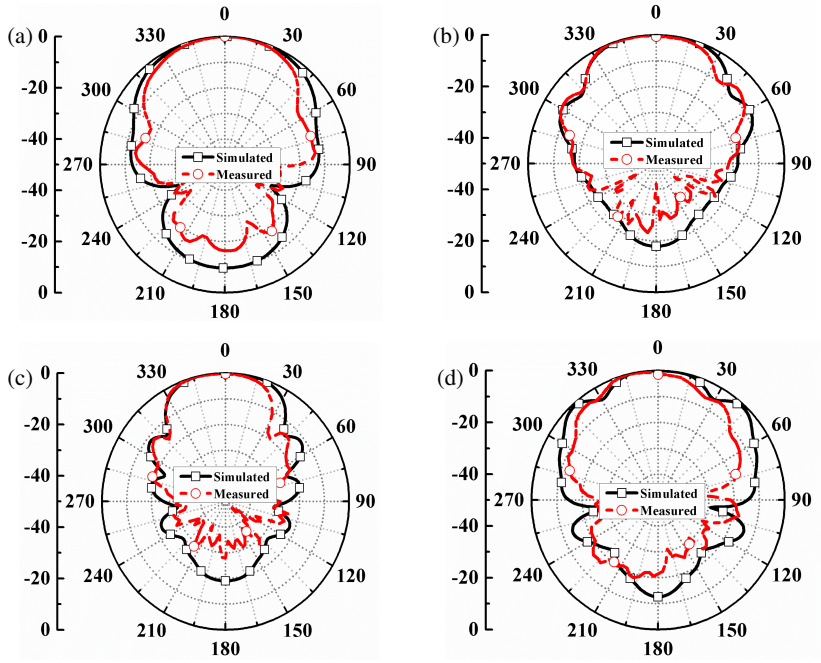

FIGURE 8. The simulated and measured H-plane radiation patterns of the proposed antenna at (a) 3 GHz, (b) 5 GHz, (c) 7 GHz and (d) 8 GHz.

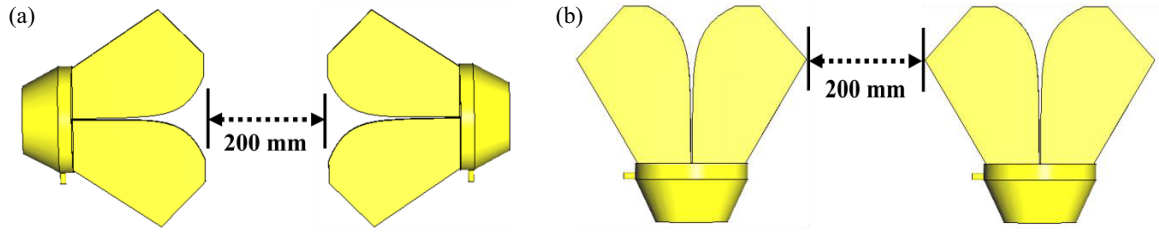

FIGURE 9. The two different antenna arrangements. (a) FTF and (b) SBS.

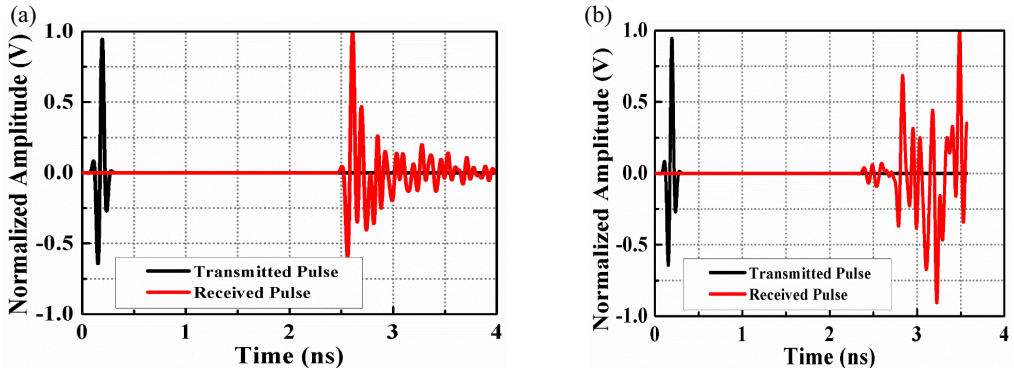

FIGURE 10. The normalized magnitude of the sent signal and received signal for two configurations. (a) FTF and (b) SBS.

3. BREAST PHANTOM DEVELOPMENT AND PERFORMANCE ASSESSMENT IN THE SIMULATOR

3.1. Breast Phantom Development in the Simulator

To conduct multiple analyses with a biological load, a realistic, heterogeneous breast phantom is designed and modeled in the simulator. The breast phantom is composed of three separate layers: the outermost layer, called the skin layer, has a radius of $R_1 = 65$ mm; the middle layer, known as the fat layer, has a radius of $R_2 = 63$ mm; and the innermost layer, referred to as the gland layer, has a radius of $R_3 = 55$ mm. Two tumors, each with a radius of $R_4 = 4$ mm, are inserted within the gland layer for testing. Fig. 12(a) shows the top view of the breast phantom; Fig. 12(b) presents the front view; and Fig. 12(c) provides the perspective view.

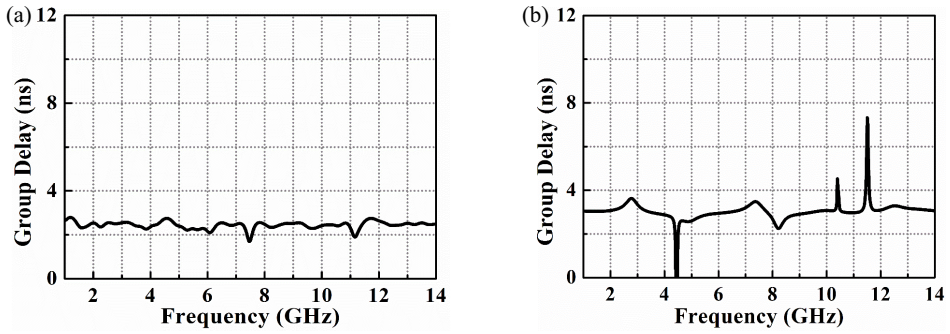

FIGURE 11. The simulated group delay for two configurations. (a) FTF and (b) SBS configuration.

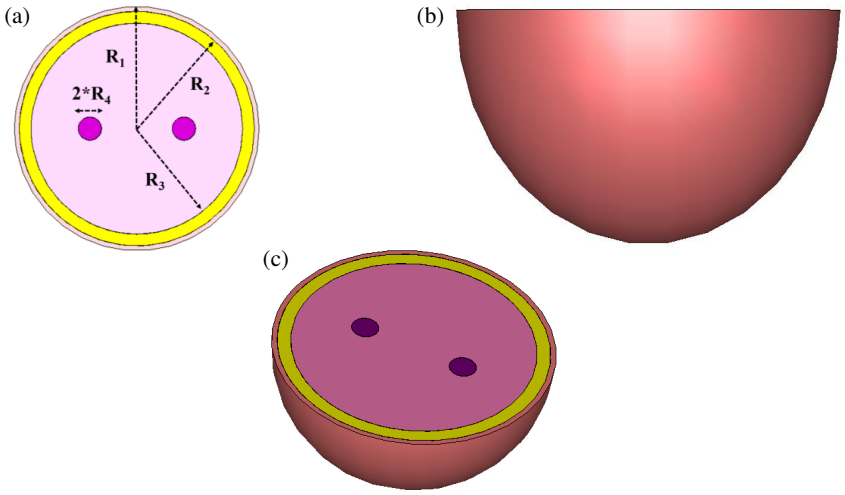

FIGURE 12. The modelled heterogeneous breast phantom in the simulator. (a) Top view, (b) Front view and (c) perspective view.

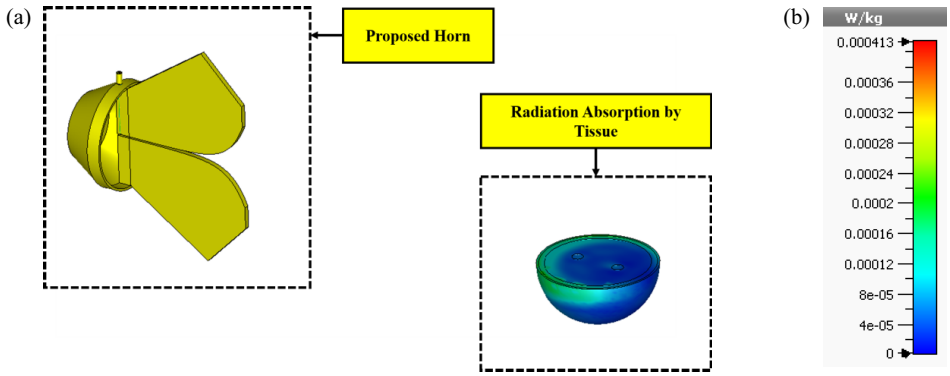

FIGURE 13. (a) The SAR assessment setup in the simulator and (b) the obtained SAR value.

3.2. SAR Assessment in the Simulator

Since the compact DRCH antenna is specifically designed for biomedical purposes, it is crucial to conduct a thorough investigation to assess electromagnetic safety. The International Commission on Non-Ionizing Radiation Protection (ICNIRP) provides widely accepted recommendations [33]. According to these standards, the maximum allowable whole-body exposure for the general population is 0.08 W/kg. For specific scenarios, such as occupational exposure or certain medical treatments (e.g., MRI), these limits may be increased [34].

To accurately assess this scenario, the maximum input power for the proposed DRCH antenna was set at 10 mW. This power level is commonly used in MI for breast cancer detection. Additionally, a test frequency of 4.2 GHz was selected, as it corresponds to the antenna's optimal impedance matching point. This selection ensures that the evaluation of SAR accounts for the most extreme scenario, where the antenna absorbs the most of the power and radiates it toward biological tissues. Fig. 13(a) illustrates the SAR assessment configuration in the CST environment, while Fig. 13(b) shows the calculated SAR value. The

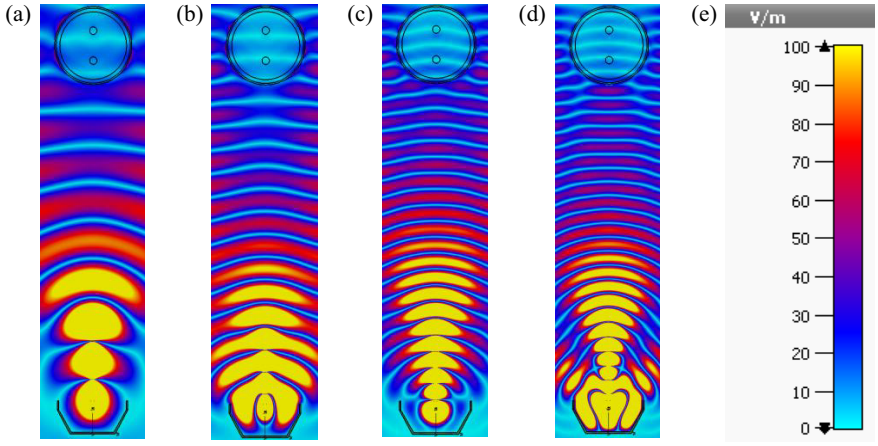

FIGURE 14. The simulated E-field distribution of the antenna with the developed breast phantom at (a) 3 GHz, (b) 5 GHz, (c) 7 GHz and (d) 8 GHz. The scaling is displayed in (e).

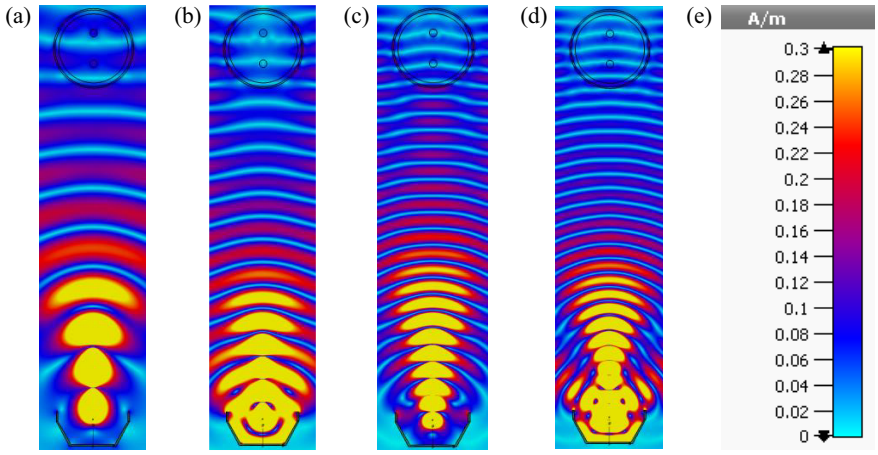

FIGURE 15. The simulated H-field distribution of the antenna with the developed breast phantom at (a) 3 GHz, (b) 5 GHz, (c) 7 GHz and (d) 8 GHz. The scaling is displayed in (e).

highest recorded SAR value is 0.4 mW/kg, which is well below the thresholds established by international regulations.

3.3. *E*-Field, *H*-Field and Power Flow Analysis with a Single Antenna in the Simulator

A thorough analysis was undertaken to evaluate the performance of the antenna for MI by assessing the penetration of both the electric field (E-field) and magnetic field (H-field) at different frequencies. Figs. 14(a)–(d) illustrate the extent to which the E-field enters the heterogeneous breast model at frequencies of 3 GHz, 5 GHz, 7 GHz, and 8 GHz, respectively. The images are depicted in the YZ plane of the antenna. Figs. 15(a)–(d) show the extent to which the H-field penetrates the identical breast model at the frequencies described earlier. The images are again depicted in the YZ plane. As breast tissues are prone to loss, the intensity of the H-field decreases as it propagates. Nevertheless, the antenna demonstrates focused propagation properties, which enhance the penetration of the electromagnetic field into the phantom. The power flow density of the antenna in the YZ plane is examined and displayed in Figs. 16(a)–(d) for the same frequencies. These figures reveal that power flows into the phantom at the observed frequencies. Through the analysis of the E-field, H-field, and power flow density at various frequencies, it is evident that the antenna can successfully penetrate the diverse composition of the breast and gather valuable data that can be further utilized for imaging.

3.4. NFD Analysis

NFD is defined as the ratio of power emitted inside the phantom (P_F) to power emitted over its surface (P_T) [32]. This phrase describes the antenna's directivity in the near field area. The NFD is calculated using Equation (3).

$$NFD = \frac{P_F}{P_T} \tag{3}$$

Fig. 17 shows the NFD plot. It can be observed that the average NFD is around 70% throughout the band.

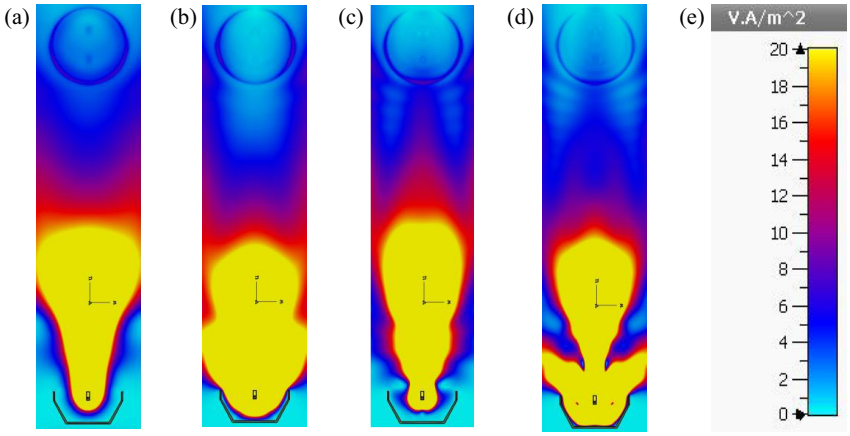

FIGURE 16. The simulated power flow density of the antenna with the developed breast phantom at (a) 3 GHz, (b) 5 GHz, (c) 7 GHz and (d) 8 GHz. The scaling is displayed in (e).

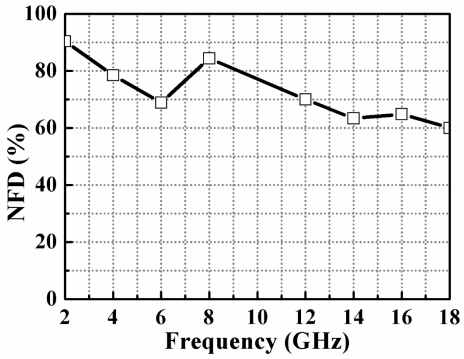

FIGURE 17. The NFD v/s frequency plot.

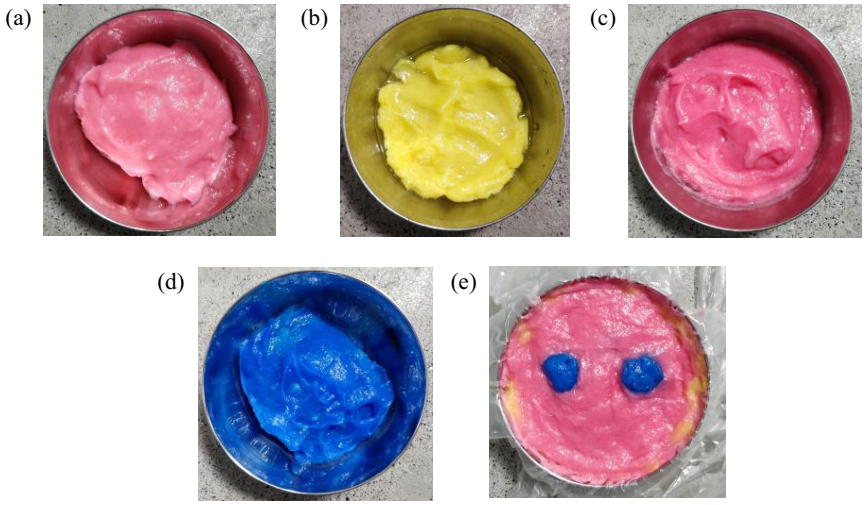

FIGURE 18. The different layers of the fabricated breast phantom. (a) Skin layer, (b) fat layer, (c) gland layer and (d) tumor layer. (e) depicts the finalized breast phantom.

4. BREAST PHANTOM FABRICATION AND IMAGING

4.1. Breast Phantom Fabrication in the Lab

The creation of the breast phantom entails many stages. Initially, propylene glycol and distilled water are mixed and heated to 50°C. Agar-agar and gelatin powder are then added and dissolved. Next, surfactant, formalin, and safflower oil are mixed, and the mixture is cooled in an ice bath before being poured into a hemispherical container to mold the skin layer. The fat layer, gland layer, and tumors are prepared similarly, but with different material concentrations. All the prepared materials are placed in separate containers after preparation. The prepared materials are depicted in Figs. 18 (a)–(d). After all the layers are prepared, they have to be placed appropriately to make the breast phantom. Initially, a hemispherical bowl is taken, and the prepared skin layer is poured into it. This is followed by pouring the fat layer into the same bowl. To create the gland layer, a portion of the hardened fat layer is removed, and the gland mixture is poured into the gap. Holes are created in the gland layer with a glass rod for the tumor mixture, which is then added. The completed phantom is refrigerated for preservation and solidification. Fig. 18(e) depicts the prepared breast phantom. The dimensions of the fabricated phantom align with the simulated model elaborated in Section 3. The phantom preparation process is based on [38], and the materials and quantities used for its fabrication are listed in Table 2.

TABLE 2. Composition of different materials for breast phantom fabrication.

Material	Quantity			
	Skin	**Fat**	**Gland**	**Tumor**
Distilled Water	120 ml	90 ml	150 ml	25 ml
Safflower Oil	21 ml	80 ml	39.375 ml	1.75 ml
Propylene glycol	10.5 ml	4.5 ml	13.125 ml	3.25 ml
Agar-Agar	8.82 g	15.75 g	9.375 g	2.25 g
Formalin	0.9 ml	1.35 g	1.125 ml	0.15 ml
Xanthan gum	2 g	2.925 g	2.4 g	0.5 g
Liquid detergent	0.9 ml	1.35 g	1.125 ml	0.15l

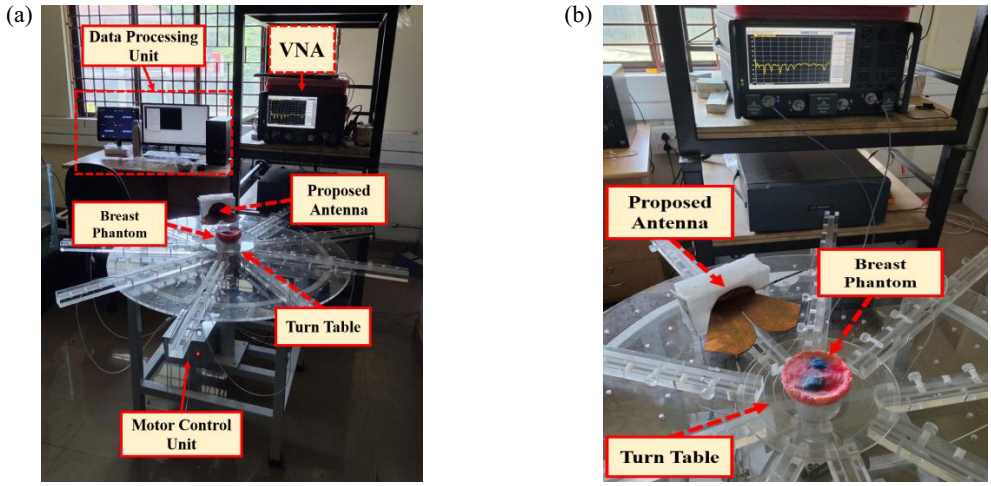

FIGURE 19. The monostatic imaging setup used in the proposed work. (a) Depicts the overall view and (b) depicts the zoomed view of the setup.

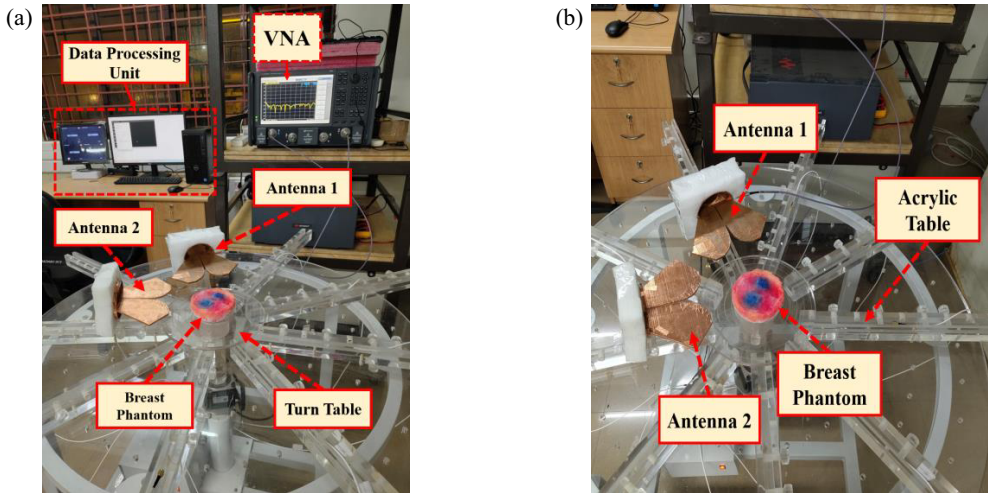

FIGURE 20. The bistatic imaging setup used in the proposed work. (a) Depicts the overall view and (b) depicts the zoomed view of the setup.

5. BREAST TUMOR DETECTION USING IMAGING ALGORITHMS

Figures 19 and 20 showcase the complete imaging setup employed in this work. Fig. 19(a) depicts the imaging setup for monostatic configuration, and Fig. 19(b) depicts the zoomed view of the antenna arrangement in this case. Fig. 20(a) depicts the imaging setup for bistatic configuration, and Fig. 20(b) depicts the zoomed view of the antenna arrangement in this case. Initially, a monostatic approach is used for image reconstruction. After the imaging process is done with a monostatic configuration, breast phantom is imaged using a bistatic arrangement as depicted in Fig. 20. In the initial stage, the breast phantom is placed on the turntable of the imaging setup. The proposed 3D printed horn antenna is positioned near the breast phantom so as to obtain necessary signals for image reconstruction, as shown in Fig. 19. The phantom is rotated in 40-degree steps to obtain a total of nine sets of readings per rotation from the VNA, which are serially stored on the connected computer. In this setup, the same antenna functions as both the transmitter and receiver. The frequency domain data (S_{11} data) corresponding to each rotation is extracted from the VNA. The widely used DAS algorithm is used to verify the imaging capability of the proposed 3D printed horn antenna. After this, another horn antenna is placed near the initial horn antenna, as depicted in Fig. 20, creating the bistatic antenna configuration. The same data retrieval steps are followed as explained previously. The primary difference here is that for the bistatic configuration, the S_{21} data is recorded as the frequency domain data which is converted to time domain for imaging.

For monostatic configuration, the delay is calculated using (4) as,

$$\tau\left(P_i\right) = \frac{2 * \left|T_x - P_i\right|}{C/\sqrt{\varepsilon}_r} \tag{4}$$

here, P_i is the pixel under consideration, T_x the transmitting antenna location, $|T_x - P_i|$ the distance from the pixel under

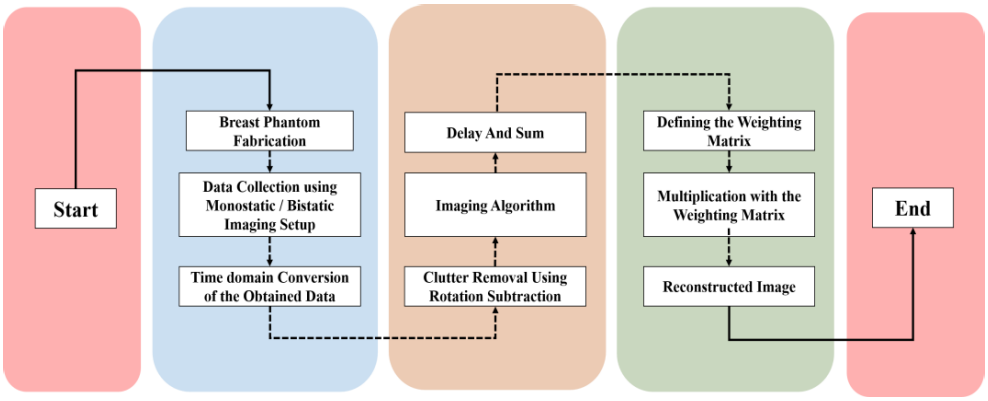

FIGURE 21. The imaging process flow chart.

observation to the transmitting antenna, C the speed of light, ε_r the dielectric constant of the layer through which the radiation is passing, and finally $\tau(P_i)$ is the calculated time delay corresponding to the pixel P_i.

For bistatic configuration, the delay is calculated using (5) as,

$$\tau\left(P_i\right) = \frac{\left|T_{a1} - P_i\right| + \left|P_i - R_{a2}\right|}{C/\sqrt{\varepsilon}_r} \tag{5}$$

Here, $|T_{a1} - P_i|$ represents the distance from the pixel under observation to 'antenna 1', and $|P_i - R_{a2}|$ represents the distance from the pixel under observation to 'antenna 2'.

During DAS, an artificial focus point is made by summing up the signals after the clutter removal procedure using rotation subtraction approach. The summed-up point exhibits higher intensity than the remaining points in the image space. The image space is visualized by plotting the intensity vs the position in MATLAB environment to display the images. The fundamental DAS algorithm is represented as (6),

$$Y_{DAS} = \sum_{I=1}^{M} \left|b_i(t - \tau)\right| \tag{6}$$

where Y_{DAS} is the DAS signal, $b_i(t-\tau)$ the delay compensated signal, and M the number of received signals.

Once the image is formed, a weighting procedure is applied to filter out the high intensity regions in the image. The complete weighting process for filtering out the image is as follows.

The image obtained with the DAS approach is assumed to be 'I' with dimensions $M \times N$. The steps for the weighting approach are as follows:

Step 1. Identify the high intensity points in the image. This is performed as shown in Equation (7).

$$H\left(i,j\right) = \begin{cases} 1, & if\ I\left(i,j\right) > T \\ 0, & otherwise \end{cases} \tag{7}$$

where T is the high intensity threshold, and H is a binary mask of high intensity points.

Step 2. Define weights for different sets of points.

- W_{high}: weight for high-intensity points.
- W_{medium}: weight for immediate neighbors.
- W_{low}: weight for the next set of neighbors.

Step 3. Creation of the weighting matrix 'W'. The weights are assigned to the pixels based on Equation (8).

$$W(i,j) = \begin{cases} w_{\text{high}} & if\ H(i,j) = 1 \\ w_{\text{medium}} & if\ \exists(i',j')\ such\ that\ H(i',j') = 1 \\ & and\ (i,j) \in\ neighbors\ (i',j'). \\ w_{\text{low}} & if\ \exists(i',j')\ such\ that\ H(i',j') = 1 \\ & and\ (i,j) \in next\ neighbor \\ 0 & otherwise \end{cases} \tag{8}$$

where 'neighbors $(i',j')'$ includes the immediate adjacent pixels of (i',j') (top, bottom, left and right), and 'next neighbors $(i',j')'$ includes the diagonal adjacent pixels.

Step 4. Multiplication of the weighting matrix with the image formed using the DAS approach, as expressed in Equation (9).

$$I_{\text{weighted}}(i,j) = I(i,j) \cdot W(ij) \tag{9}$$

Step 5. Normalization of the the weighted image to get the final image. The equation is depicted by (10).

$$I_{\text{final}}(i,j) = \frac{I_{\text{weighted}}(i,j)}{\max\left(I_{\text{weighted}}\right)} \tag{10}$$

Combining all these steps, the full mathematical expression for each pixel (i,j) in the weighted image is depicted by (11) as

$$I_{\text{final}}(i,j) = \frac{I(i,j) \cdot W(i,j)}{\max(I(i,j) \cdot W(i,j))} \tag{11}$$

This approach ensures that the areas with higher intensities and their nearby pixels are assigned higher weights, with the possibility to control the intensity of weighting through the parameters w_{high}, w_{medium}, and w_{low}.

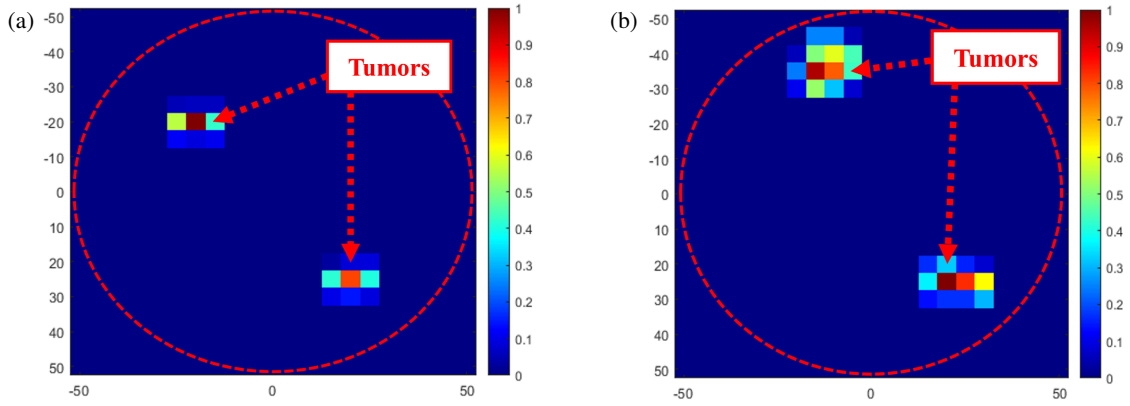

FIGURE 22. The reconstructed image of the breast phantom using (a) monostatic approach and (b) bistatic approach.

TABLE 3. The performance comparison of the proposed DRCH with similar works in literature.

Reference	Antenna Type	Technology	Overall Size (mm^3)	Volume $(mm)^3$	Bandwidth (GHz)	Weight (Kg)
[31]	Dual Ridged Horn	Metallic	240 × 137 × 212	69, 70, 560	0.8–20	NM
[35]	Dual Ridged Horn	Metallic	240 × 138 × 152.5	50, 50, 800	1–14	Simulated
[36]	Dual Ridged Horn	Metallic	184 × 126 × 112	25, 96, 608	1–18	Simulated
[26]	Dual Ridged Horn	Metallic	243 × 154 × 200	74, 84, 400	1–18	0.8
[37]	Dual Ridged Horn	Metallic	151 × 108 × 146.6	23, 90, 752.8	1–9	0.3
This Work	**Dual Ridge Conical Horn**	**3D printing**	**193.8 × 95 × 122.3**	**22, 51, 665.3**	**0.69–12**	**0.13475**

NM — Not Mentioned

The complete imaging process in this work is represented in the form of a flowchart as displayed in Fig. 21. The reconstructed image of the fabricated breast phantom with two tumors using the monostatic approach is depicted in Fig. 22(a), and the image using the bistatic approach is depicted in Fig. 22(b). The embedded tumors are appropriately identified up to a reasonable extent. Minor deviations from the exact tumor locations as well as their shape is observed. This can be attributed to measurement errors during data collection with the phantoms, irregular placement of the phantom on the turntable, RF switch losses, and scaling differences in the algorithm weighting.

The work done in this study is compared to some of the recent works in the literature which is listed in Table 3. It is evident that the proposed work utilizes 3D printing technology to fabricate the conical horn antenna. The overall volume of the proposed antenna is lower than other works, and the proposed antenna weighs the least among the existing designs. Furthermore, the proposed work is unique in using a 3D-printed horn antenna for image reconstruction of a heterogeneous breast phantom using both monostatic and bistatic approaches.

6. CONCLUSION

The proposed work introduces a 3D-printed DRCH antenna for MI. The antenna operates between 0.69 and 12 GHz and has a peak gain of 14 dBi at 12 GHz. The frequency and time-domain characteristics are thoroughly examined. A heterogeneous breast phantom with two tumors is modeled in the simulator and later fabricated in the laboratory. The proposed antenna is initially subjected to SAR analysis using the simulated breast phantom. The antenna is then employed to reconstruct the tumors embedded in the fabricated breast phantom. The phantom is scanned using both monostatic and bistatic methods. Initially, the fundamental DAS technique is applied, followed by a novel weighting approach for determining peak intensities and filtering out undesirable clutter. The tumors are clearly detected using both the monostatic and bistatic approaches. In the future, the proposed antenna will be utilized in conjunction with different algorithms to image a variety of complex heterogeneous breast phantoms. Additionally, multiple clutter reduction methods will be combined with this effort to reduce false-positive intensities and pinpoint the actual positions of the targets. The constructed antenna will also be employed for nondestructive testing in the future.

ACKNOWLEDGEMENT

The authors would like to express their profound gratitude to the IIT Mandi iHUB and HCI foundation under project number IIT MANDI iHub/RD/2023-2025/03 and Science and Engineering Research Board, Government of India under project number TTR/2022/000001, for partially funding of this work. The authors would also like to thank the Director of Indian Institute of Technology Palakkad for setting up the Central Instrumentation Facility.

COMPETING INTERESTS

The authors declare that there are no conflicts of interest.

REFERENCES

[1] Modiri, A., S. Goudreau, A. Rahimi, and K. Kiasaleh, "Review of breast screening: Toward clinical realization of microwave imaging," *Medical Physics*, Vol. 44, No. 12, e446–e458, 2017.

[2] Kwon, S. and S. Lee, "Recent advances in microwave imaging for breast cancer detection," *International Journal of Biomedical Imaging*, Vol. 2016, No. 1, 5054912, Dec. 2016.

[3] Persson, M., A. Fhager, H. D. Trefná, Y. Yu, T. McKelvey, G. Pegenius, J.-E. Karlsson, and M. Elam, "Microwave-based stroke diagnosis making global prehospital thrombolytic treatment possible," *IEEE Transactions on Biomedical Engineering*, Vol. 61, No. 11, 2806–2817, 2014.

[4] Mobashsher, A. T., A. M. Abbosh, and Y. Wang, "Microwave system to detect traumatic brain injuries using compact unidirectional antenna and wideband transceiver with verification on realistic head phantom," *IEEE Transactions on Microwave Theory and Techniques*, Vol. 62, No. 9, 1826–1836, Sep. 2014.

[5] Ljungqvist, J., S. Candefjord, M. Persson, L. Jönsson, T. Skoglund, and M. Elam, "Clinical evaluation of a microwave-based device for detection of traumatic intracranial hemorrhage," *Journal of Neurotrauma*, Vol. 34, No. 13, 2176–2182, 2017.

[6] Rezaeieh, S. A., K. S. Bialkowski, and A. M. Abbosh, "Microwave system for the early stage detection of congestive heart failure," *IEEE Access*, Vol. 2, 921–929, 2014.

[7] Chandra, R., H. Zhou, I. Balasingham, and R. M. Narayanan, "On the opportunities and challenges in microwave medical sensing and imaging," *IEEE Transactions on Biomedical Engineering*, Vol. 62, No. 7, 1667–1682, Jul. 2015.

[8] Mahmud, M. Z., M. T. Islam, N. Misran, A. F. Almutairi, and M. Cho, "Ultra-wideband (UWB) antenna sensor based microwave breast imaging: A review," *Sensors*, Vol. 18, No. 9, 2951, 2018.

[9] Aldhaeebi, M. A., K. Alzoubi, T. S. Almoneef, S. M. Bamatraf, H. Attia, and O. M. Ramahi, "Review of microwaves techniques for breast cancer detection," *Sensors*, Vol. 20, No. 8, 2390, 2020.

[10] O'Loughlin, D., M. O'Halloran, B. M. Moloney, M. Glavin, E. Jones, and M. A. Elahi, "Microwave breast imaging: Clinical advances and remaining challenges," *IEEE Transactions on Biomedical Engineering*, Vol. 65, No. 11, 2580–2590, Nov. 2018.

[11] Bourqui, J., M. A. Campbell, T. Williams, and E. C. Fear, "Antenna evaluation for ultra-wideband microwave imaging," *International Journal of Antennas and Propagation*, Vol. 2010, No. 1, 850149, May 2010.

[12] Khor, W. C., M. E. Bialkowski, A. Abbosh, N. Seman, and S. Crozier, "An ultra wideband microwave imaging system for breast cancer detection," *IEICE Transactions on Communications*, Vol. 90, No. 9, 2376–2381, 2007.

[13] O'Halloran, M., M. Glavin, and E. Jones, "Rotating antenna microwave imaging system for breast cancer detection," *Progress In Electromagnetics Research*, Vol. 107, 203–217, 2010.

[14] Conceicao, R. C., M. O'Halloran, M. Glavin, and E. Jones, "Comparison of planar and circular antenna configurations for breast cancer detection using microwave imaging," *Progress In Electromagnetics Research*, Vol. 99, 1–20, 2009.

[15] Fasoula, A., L. Duchesne, J. D. G. Cano, P. Lawrence, G. Robin, and J.-G. Bernard, "On-site validation of a microwave breast imaging system, before first patient study," *Diagnostics*, Vol. 8, No. 3, 53, 2018.

[16] Preece, A. W., I. Craddock, M. Shere, L. Jones, and H. L. Winton, "MARIA M4: Clinical evaluation of a prototype ultrawideband radar scanner for breast cancer detection," *Journal of Medical Imaging*, Vol. 3, No. 3, 033502, 2016.

[17] Hassan, N. A., M. M. Mohamed, and M. B. Tayel, "Basic evaluation of antennas used in microwave imaging for breast cancer detection," *Computer Science & Information Technology (CS & IT)*, Vol. 55, 55–63, 2016.

[18] Balanis, C. A., *Antenna Theory: Analysis and Design*, John Wiley & Sons, Hoboken, NJ, USA, 2015.

[19] Giampietri, E., D. Brizi, A. Monorchio, and N. Fontana, "Miniaturized antennas design for microwave imaging applications," in *2020 IEEE International Symposium on Antennas and Propagation and North American Radio Science Meeting*, 537–538, Montreal, QC, Canada, Jul. 2020.

[20] Alibakhshikenari, M., B. S. Virdee, P. Shukla, N. O. Parchin, L. Azpilicueta, C. H. See, R. A. Abd-Alhameed, F. Falcone, I. Huynen, T. A. Denidni, and E. Limiti, "Metamaterial-inspired antenna array for application in microwave breast imaging systems for tumor detection," *IEEE Access*, Vol. 8, 174 667–174 678, 2020.

[21] Althuwayb, A. A., "Enhanced radiation gain and efficiency of a metamaterial-inspired wideband microstrip antenna using substrate integrated waveguide technology for sub-6 GHz wireless communication systems," *Microwave and Optical Technology Letters*, Vol. 63, No. 7, 1892–1898, 2021.

[22] Althuwayb, A. A., "MTM-and SIW-inspired bowtie antenna loaded with AMC for 5G mm-Wave applications," *International Journal of Antennas and Propagation*, Vol. 2021, No. 1, 6658819, Jan. 2021.

[23] Alibakhshikenari, M., F. Babaeian, B. S. Virdee, S. Aïssa, L. Azpilicueta, and C. H. See, "A comprehensive survey on "Various decoupling mechanisms with focus on metamaterial and metasurface principles applicable to SAR and MIMO antenna systems"," *IEEE Access*, Vol. 8, 192 965–193 004, 2020.

[24] Alibakhshi-Kenari, M., M. Naser-Moghadasi, and R. Sadeghzadeh, "The resonating MTM-based miniaturized antennas for wide-band RF-microwave systems," *Microwave and Optical Technology Letters*, Vol. 57, No. 10, 2339–2344, 2015.

[25] Rezaeieh, S. A., A. Zamani, K. S. Bialkowski, A. Mahmoud, and A. M. Abbosh, "Feasibility of using wideband microwave system for non-invasive detection and monitoring of pulmonary oedema," *Scientific Reports*, Vol. 5, No. 1, 14047, 2015.

[26] "DRH18-E double ridged waveguide horn," (Accessed on Dec. 2020). [Online]. Available: https://www.rfspin.cz/en/antennas/measurement-antennas/drh18e.

[27] Schwarzbeck Mess-Elektronik, "BBHA 9120 F — Double ridged broadband horn antenna," (Accessed on Dec. 2020). [Online]. Available: http://www.schwarzbeck.de/en/antennas/broadband-horn-antennas/double-ridged-horn-antenna/406-bbha-9120-fdouble-ridged-broadband-horn-antenna.html.

[28] Asok, A. O., S. J. G. Nath, A. Tripathi, S. Chauhan, K. S. Kiran, and S. Dey, "Double ridge conical horn antenna with dielectric loading for microwave imaging of human breast," in *2022 IEEE Wireless Antenna and Microwave Symposium (WAMS)*, 1–4, Rourkela, India, 2022.

[29] Ghavami, N., G. Tiberi, D. J. Edwards, and A. Monorchio, "UWB microwave imaging of objects with canonical shape," *IEEE Transactions on Antennas and Propagation*, Vol. 60, No. 1, 231–239, Jan. 2012.

[30] Abbas-Azimi, M., F. Arazm, and R. Faraji-Dana, "Design and optimisation of a high-frequency EMC wideband horn antenna," *IET Microwaves, Antennas & Propagation*, Vol. 1, No. 3, 580–585, 2007.

[31] Wang, C., E. Li, Y. Zhang, and G. Guo, "Ridged horn antenna with adjustable metallic grid sidewalls and cross-shaped back cavity," *IEEE Antennas and Wireless Propagation Letters*, Vol. 15, 1221–1225, 2015.

[32] Talukder, M. S., M. Samsuzzaman, M. T. Islam, R. Azim, M. Z. Mahmud, and M. T. Islam, "Compact ellipse shaped patch with ground slotted broadband monopole patch antenna for head imaging applications," *Chinese Journal of Physics*, Vol. 72, 310–326, 2021.

[33] Ahlbom, A., U. Bergqvist, J. H. Bernhardt, J. P. Cesarini, M. Grandolfo, M. Hietanen, A. F. Mckinlay, M. H. Repacholi, D. H. Sliney, *et al.*, "Guidelines for limiting exposure to time-varying electric, magnetic, and electromagnetic fields (up to 300 GHz)," *Health Physics*, Vol. 74, No. 4, 494–521, 1998.

[34] Canicattì, E., E. Giampietri, D. Brizi, N. Fontana, and A. Monorchio, "A numerical exposure assessment of portable self-protection, high-range, and broadband electromagnetic devices," *IEEE Open Journal of Antennas and Propagation*, Vol. 2, 555–563, 2021.

[35] Botello-Perez, M., H. Jardon-Aguilar, and I. G. Ruiz, "Design and simulation of a 1 to 14 GHz broadband electromagnetic compatibility DRGH antenna," in *2005 2nd International Conference on Electrical and Electronics Engineering*, 118–121, Mexico City, Mexico, Sep. 2005.

[36] Bruns, C., P. Leuchtmann, and R. Vahldieck, "Analysis and simulation of a 1-18-GHz broadband double-ridged horn antenna," *IEEE Transactions on Electromagnetic Compatibility*, Vol. 45, No. 1, 55–60, Feb. 2003.

[37] Diana, S., D. Brizi, C. Ciampalini, G. Nenna, and A. Monorchio, "A compact double-ridged horn antenna for ultra-wide band microwave imaging," *IEEE Open Journal of Antennas and Propagation*, Vol. 2, 738–745, 2021.

[38] Islam, M. T., M. Samsuzzaman, S. Kibria, and M. T. Islam, "Experimental breast phantoms for estimation of breast tumor using microwave imaging systems," *IEEE Access*, Vol. 6, 78 587–78 597, 2018.